www.neurosci.cn

CrossMark

ORIGINAL ARTICLE

The Glutamatergic Postrhinal Cortex–Ventrolateral Orbitofrontal Cortex Pathway Regulates Spatial Memory Retrieval

Xinyang Qi[1] · Zhanhong Jeff Du[2] · Lin Zhu[1] · Xuemei Liu[2] · Hua Xu[1] ·
Zheng Zhou[2] · Cheng Zhong[2] · Shijiang Li[3] · Liping Wang[2] · Zhijun Zhang[1,2]

Abstract A deficit in spatial memory has been taken as an early predictor of Alzheimer's disease (AD) or mild cognitive impairment (MCI). The uncinate fasciculus (UF) is a long-range white-matter tract that connects the anterior temporal lobe with the orbitofrontal cortex (OFC) in primates. Previous studies have shown that the UF impairment associated with spatial memory deficits may be an important pathological change in aging and AD, but its exact role in spatial memory is not well understood. The pathway arising from the postrhinal cortex (POR) and projecting to the ventrolateral orbitofrontal cortex (vlOFC) performs most of the functions of the UF in rodents. Although the literature suggests an association between spatial memory and the regions connected by the POR–vlOFC pathway, the function of the pathway in spatial memory is relatively unknown. To further illuminate the function of the UF in spatial memory, we dissected the POR–vlOFC pathway in mice. We determined that the POR–vlOFC pathway is a glutamatergic structure, and that glutamatergic neurons in the POR regulate spatial memory retrieval. We also demonstrated that the POR–vlOFC pathway specifically transmits spatial information to participate in memory retrieval. These findings provide a deeper understanding of UF function and dysfunction related to disorders of memory, as in MCI and AD.

Keywords Spatial memory · Postrhinal cortex · Ventrolateral orbitofrontal cortex · Mild cognitive impairment · Alzheimer's disease

Xinyang Qi, Zhanhong Jeff Du and Lin Zhu have contributed equally to this work.

✉ Liping Wang
  lp.wang@siat.ac.cn

✉ Zhijun Zhang
  janemengzhang@vip.163.com

[1] Department of Neurology, Affiliated ZhongDa Hospital, Institute of Neuropsychiatry, School of Medicine, Southeast University, Nanjing 210009, China

[2] Shenzhen Key Lab of Neuropsychiatric Modulation and Collaborative Innovation Center for Brain Science, Chinese Academy of Sciences (CAS) Center for Excellence in Brain Science and Intelligence Technology, the Brain Cognition and Brain Disease Institute for Collaboration Research of the Shenzhen Institutes of Advanced Technology at the CAS and the McGovern Institute at Massachusetts Institute of Technology, Shenzhen 518055, China

[3] Department of Biophysics, Medical College of Wisconsin, Milwaukee, WI 53226, USA

Introduction

Spatial memory refers to the part of the memory system which is in charge of encoding, storing and recalling spatial information about the environment and the objects and agents within it [1]. Spatial memory is required for individuals to navigate to goal locations and is vitally important for reaching goals in a spatially extended environment [1, 2]. Patients with a spatial memory deficit often show disorientation, which is the core symptom in emerging mild cognitive impairment (MCI) and the early stage of Alzheimer's disease (AD) [3–5]. Illuminating the working mechanism of spatial memory may contribute to further understanding of the pathology of these diseases. However, the neural mechanism of spatial memory is not well understood. Functional magnetic resonance imaging (fMRI) has suggested that the temporal [6], frontal [7], and occipital lobes [3] are the critical areas in the neural circuit for spatial memory, but details regarding the function of

448

Neurosci. Bull. June, 2019, 35(3):447–460

these areas and fiber tracts in spatial memory remain to be elucidated.

The uncinate fasciculus (UF) is a long-range white-matter fiber tract connecting the anterior temporal lobe with the orbitofrontal cortex (OFC), a subregion of the frontal lobe, through a direct, monosynaptic pathway [8]. The temporal segment of the tract originates from the anterior part of the parahippocampal cortex and the temporal pole [9]. The UF belongs to a small group of late-myelinating white matter association tracts that undergo protracted development throughout adolescence [10]. So, this slow maturation may open a time window during which these fibers are more vulnerable to risk factors causing neurological and psychotic disorders [8]. The exact function of the UF remains unclear, but diffusion tensor imaging (DTI) studies have indicated that microstructural deficits of the UF occur in such conditions as anxiety [11], depression [12], schizophrenia [13], psychopathy [14], frontotemporal dementia [15], MCI [16], and AD [17]. Furthermore, some task-fMRI and DTI studies have shown that UF dysfunction is associated with age-related impairment of spatial navigation [18] and spatial memory deficits in MCI [19]. Nevertheless, it remains unclear how the UF participates in spatial memory processing; particularly in the encoding, storage, or retrieval stage of spatial memory.

The postrhinal cortex (POR) is the rodent homolog of the primate parahippocampal cortex [20]. Previous studies have confirmed that the POR is rich in GABAergic and glutamatergic neurons [21], and is strongly connected with the visual area, laterodorsal thalamic nucleus (LD), hippocampal formation, caudate-putamen, and prefrontal cortex (PFC) [22–24]. As a core region of the PFC, the ventrolateral orbitofrontal cortex (vlOFC) mainly receives projections from the POR which may contribute to UF function in rodents [20]. POR/OFC lesions cause spatial memory impairment in rodents [25, 26], suggesting that both the POR and OFC are key regions in the neural circuit of spatial memory. However, the function of the POR–vlOFC pathway connecting the two regions in spatial memory has not been investigated in rodents, and its structure remains to be elucidated.

To further illuminate the function of the UF in spatial memory, we set out to dissect the POR–vlOFC pathway in mice. We aimed to examine the structure of the POR–vlOFC pathway and its exact function in spatial memory.

Methods

Animals

Adult (20 g–30 g) male C57BL/6 mice (Guangdong Medical Laboratory Animal Center, Guangzhou, China), and adult male GAD2-Cre mice aged 6 weeks–8 weeks at the beginning of experiments, were housed in groups of five per cage. The GAD2-Cre mice had Cre recombinase expression directed to GAD2-positive neurons without disrupting endogenous glutamic acid decarboxylase 2 expression. The animals were maintained on a 12/12-h light/dark cycle (lights on at 08:00, Beijing time) at a stable temperature (23°C–25°C) and given food and water *ad libitum*. All animal experiments were approved by the Institutional Animal Care and Use Committee of Shenzhen Institutes of Advanced Technology, Chinese Academy of Sciences.

Anatomy of the POR

The POR is bordered by the following structures: the caudal end of the angular bundle, the caudal part of the perirhinal cortex [27], the ventral temporal association area (TEA), and the dorsal part of the medial entorhinal cortex (Fig. 1A). The POR is bordered rostrally by the perirhinal cortex, which was identified by subicular cells in the angular bundle [21, 28]. The POR was differentiated from the TEA by identification of discrete layers II, III, and IV, and the bilaminate appearance of layer V. The POR lies above a slight indentation surrounded by the medial entorhinal cortex. In the coronal plane (Fig. 1B–D), the POR was identified as the region bordered by the rhinal fissure rostrally and medially, and the TEA at the middle of the angular bundle dorsally. At caudal levels, the POR is triangular in shape. The dorsal portion is bordered by the parasubiculum, which forms one side of a triangle together with the entorhinal. TEA forms the second side, and the cortical surface, the third side.

Immunofluorescence Staining

Mice were anesthetized with chloral hydrate (10% *w/v*, 300 mg/kg body weight) and perfused transcardially with phosphate-buffered saline (PBS) followed by ice-cold 4% paraformaldehyde (PFA, 158127 MSDS, Sigma, St. Louis, MO) (mice for c-fos staining were sacrificed 1.5 h after blue light stimulation). The brain was removed carefully and post-fixed in 4% PFA at 4 °C overnight, then cryoprotected in PBS containing 25% sucrose for 48 h. Coronal sections (40 μm) were cut on a Leica (Wetzlar, Germany) freezing microtome. Free-floating sections were
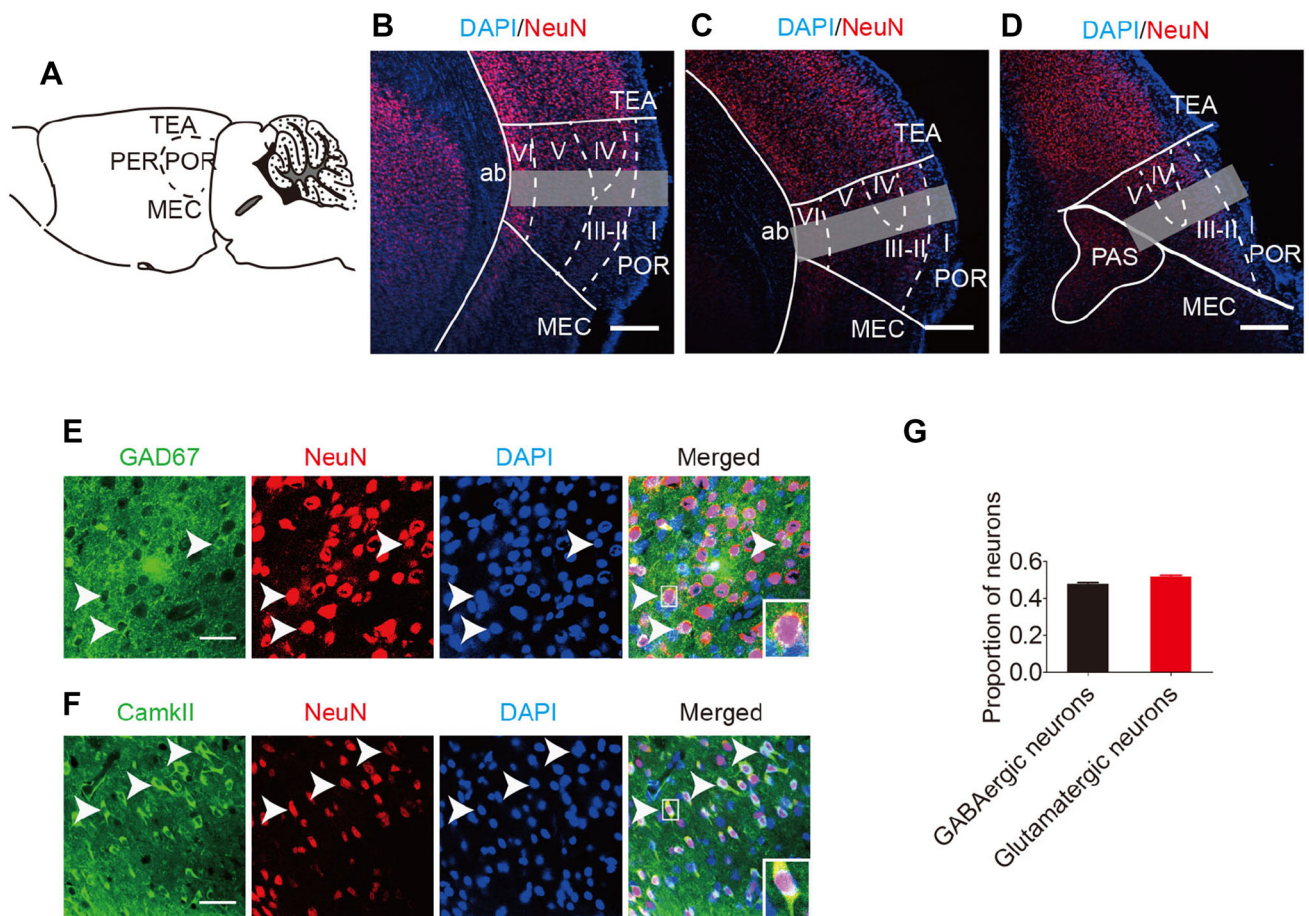
Fig. 1 Identification of postrhinal cortex (POR) borders and neuronal composition in the mouse. **A** Lateral surface view of the POR borders. **B–D** Schematic of the POR shows 3 rostrocaudal levels in the coronal plane. Gray rectangles indicate the cell-counting regions (scale bars, 250 μm). AP: **B**, −4.70 mm; **C**, −4.85 mm; **D**, −5.00 mm. TEA, temporal association area; PER, perirhinal cortex; Entl, lateral entorhinal area; PAS, parasubiculum area. **E, F** POR neurons co-labeled for (**E**) GAD67 (green) and NeuN (red) or (**F**) CamkII (green) and NeuN (red) are indicated by arrowheads (scale bars, 50 μm). **G** Proportions of GABAergic (48.4% ± 1.6%) and glutamatergic (51.4% ± 1.8%) neurons in the POR. Data are presented as mean ± SEM.

rinsed with PBS on a rocking bed (60 rpm, 10 min × 3 times), and incubated in 0.3% TritonX-100 and 10% normal goat serum (Jackson) in PBS for 1 h at room temperature. Sections were then incubated overnight in primary antibody with 1% bovine serum albumin and 0.1% TritonX-100. The antibodies were rabbit monoclonal anti-NeuN (dilution 1:200, 2625391; Millipore, Billerica, MA); mouse monoclonal anti-GAD67 (1:100, MAB1572; Millipore); mouse monoclonal anti-CamKII (1:250, ab22609, Abcam, Cambridge, UK), and rabbit monoclonal anti-c-fos (1:200, 2250; Cell Signaling). After thorough washing with PBS, the sections were incubated with the secondary antibodies at room temperature for 3 h. The antibodies were Alexa fluor 488 or 594 goat anti-rabbit IgG and Alexa fluor 488 or 594 goat anti-mouse IgG (1:100, Jackson). After washing with PBS (15 min × 3 times), the sections were mounted on gelatin-coated slides and coverslipped with an anti-fade reagent and DAPI (Image-iT FX Signal

Enhancer, Invitrogen). The sections were then photographed and analyzed with a Leica TCS SP5 laser scanning confocal microscope.

Cell Quantification

To determine the cell types in the POR, 3 coronal sections per mouse (*n* = 3) from the POR on one side (AP from −4.60 mm to −5.10 mm, spaced 120 μm apart) were examined (Fig. 1B–D). Cell-type identification was quantified using a confocal microscope (63 × objective) by the cell-type-specific staining of NeuN immunoreactive cells. Cells were counted manually using ImageJ.

To quantify c-fos-positive cells, 4 coronal sections per mouse (*n* = 3) from the bilateral vlOFC (AP from 2.80 mm to 2.00 mm, spaced 300 μm apart) were examined. Confocal images (10× objective) were acquired using identical pinhole, gain, and laser settings. Cells were counted

450

Neurosci. Bull. June, 2019, 35(3):447–460

automatically using Image pro plus software. To determine the types of c-fos-positive cells, a confocal microscope (63× objective) was used to compare the cell-type-specific staining with c-fos. Cells were counted manually using ImageJ.

Virus Injection and Optic Fiber Implantation

Mice were anesthetized with pentobarbital sodium (0.5% w/v, 80 mg/kg body weight, i.p.) (Merck, Darmstadt, Germany), then placed in a stereotaxic apparatus (RWD, Shenzhen, China). Erythromycin eye ointment was used to keep the corneas wet and a heating pad (RWD) was used to maintain body temperature. A small incision was made to expose the skull surface and to visualize bregma and lambda. A dental drill (RWD) was used to drill holes on the skull surface. AAV5-CaMKIIα-mCherry or AAV5-CaMKIIα-eNpHR3.0-mCherry was injected into the bilateral POR (AP: −4.84 mm, ML: ± 3.80 mm, DV: −2.25 mm) for optical inhibition experiments; AAV5-CaMKIIα-mCherry or AAV5-CaMKIIα-hChR2-mCherry was injected into the unilateral POR (AP: −4.84 mm, ML: 3.80 mm, DV: −2.25 mm) for optical activation experiments. Virus was injected into the POR (0.4 μL at 80 nL/min) through a 10-μL microsyringe with a 33-gauge metal needle (Neuros; Hamilton, Reno, NV) connected to a microsyringe pump (UMP3; WPI, Sarasota, FL) and its controller (Micro4; WPI). After the injection finished, the needle was left in place for an extra 5 min and then withdrawn slowly.

An optic fiber was implanted 6 weeks after virus injection. For optogenetic stimulation of POR somata, an optic fiber (Numerical aperture = 0.37, φ = 200 μm; Shanghai Fiblaser Technology Co., Ltd, Shanghai, China) was inserted into the POR (AP: −4.84 mm, ML: ± 3.80 mm, DV: −1.75 mm). To stimulate terminals, the fiber was implanted in the vlOFC (AP: 2.10 mm, ML: ± 1.50 mm, DV: −3.25 mm), LD (AP: −1.35 mm, ML: ± 1.25 mm, DV: −2.30 mm), or dorsal hippocampal commissure (DHC) (AP: −3.40 mm, ML: ± 1.50 mm, DV: −1.25 mm) to target *Natronomonas* halorhodopsin (eNpHR3.0)-containing terminals projecting to the POR. Implants were fixed to the skull with a layer of cyanoacrylate (Permabond, Englewood, CO) and covered by dental cement (New Century, Shanghai, China). After the surgery, the skin was sutured and lidocaine hydrochloride gel and lincomycin hydrochloride were used to prevent inflammation and control pain.

Anterograde Tracing

Virus-delivered trackers were injected into the POR on one side. Six weeks later, mice were anaesthetized with a lethal dose of chloral hydrate and perfused transcardially with PBS, followed by ice-cold 4% paraformaldehyde. Coronal brain sections (40 μm) were cut on the Leica freezing microtome. Free-floating sections were rinsed with PBS on a rocking bed (60 rpm, 10 min × 3 times). The sections were then mounted on gelatin-coated slides and cover-slipped with an anti-fade reagent containing DAPI. The expression of mCherry was detected on a Leica TCS SP5 laser scanning confocal microscope.

Novel Object Place Recognition

The experiments were performed in a 50 × 50 × 50 cm³ open field (made of white polyvinyl chloride). A high-definition digital camera (Sony, Shanghai, China) was used to record the animals' behavior. Mice were habituated to a testing box and the experimental procedure lasted over 4 days [29, 30]. Mice explored the empty open field for 20 min during days 1 and 2. On days 3 and 4, the mice were habituated to the box containing two identical objects. The adaptive phase included a study phase (6 min), a delay (20 min), and a recognition phase (6 min). But the objects used in the adaptive phase were different from those on the testing day. On the testing day (day 5), the task included the same sequence of study, delay, and recognition phases. During the study phase, mice were exposed to two identical objects. After the delay, the position of one of the objects was changed. The mice were then exposed to the two objects for another 6 min. During the task, each mouse received optical stimulation based on their group. After each trial, the open field and the objects were cleaned with 25% ethanol. Offline analyses were performed with video software (ANY-maze; Stoelting Co, Wood Dale, IL) and custom-designed scripts. The standard memory index (D2) was used: D2 = (exploration time$_{(novel\ object)}$ − exploration time$_{(familiar\ object)}$)/total exploration time. A D2 score > 0 reflected successful memory performance.

Optogenetic Manipulation and Behavioral Test in Freely-Moving Mice

The behavioral test was performed one week after optic fiber implantation (Fig. 2). Two implanted optic fibers were connected to a yellow light laser (MBL-589/200 mW) or one of the fibers was connected to a blue light laser (MBL-473/200 mW) *via* custom patch cords (all from Shanghai Fiblaser Technology Co., Ltd) and a fiber-optic rotary joint (Doric Lenses, Quebec, Canada) which released the torsion on the fibers due to rotation of the mouse. The power of the blue light was set at 8 mW–10 mW at the tip of the fiber for cell body stimulation and 10 mW–15 mW for terminal stimulation, while the yellow light was set at 10 mW–15 mW for cell body stimulation

Fig. 2 Implant location of fibers and expression of hChR2 and eNpHR3.0 in the POR. **A, C** hChR2 and eNpHR3.0 expression in the POR and implant location of fiber (scale bars, 750 μm). **B, D** CamkII (green) stained with hChR2 or eNpHR3.0 (red); arrowheads, co-labeled neurons. hChR2 or eNpHR3.0 expression occurred only in CamkII^{+} neurons (scale bars, 50 μm).
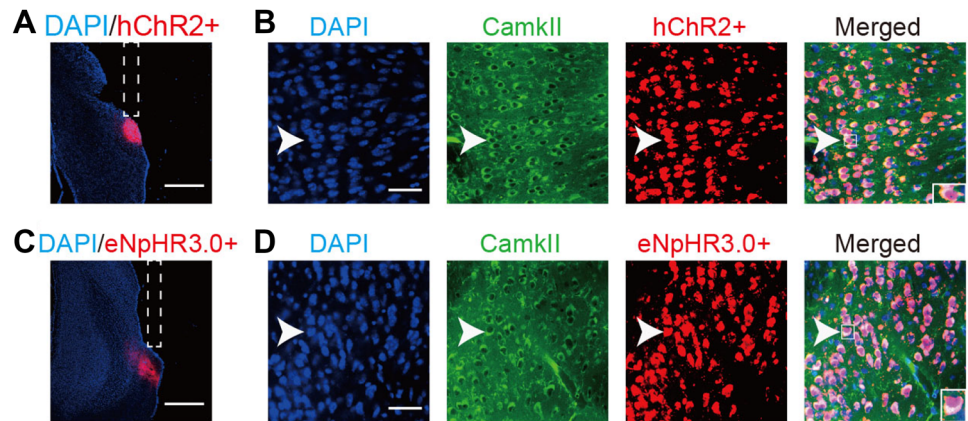
and 15 mW–20 mW for terminal stimulation. Continuous yellow laser for mice using eNpHR3.0 or 20-Hz 5 ms-pulsed blue laser for mice using *Chlamydomonas* channel-rhodopsin-2 (hChR2) was delivered during the behavioral tests.

Fabrication of Electrode Arrays for Optogenetics

Each multi-channel optrode array contained 1 optical channel and 4 twisted tetrodes (16 channels). The arrays were fabricated from optical fibers (NA = 0.37, φ = 200 μm) and formvar-coated nickel chromium wires 12-μm in diameter (Fig. 3A). Each tetrode was threaded through a silica tube (75 μm inner, 152 μm outer diameters). In the optrode array, 4 tetrodes were arranged around an optical fiber (Fig. 3A). To ensure illumination of the recorded neurons, the tips of the recording sites were 300 μm–500 μm longer than the optical fiber (Fig. 3B). Recording sites were plated with platinum to reduce the impedance to 200 kΩ–500 kΩ (at 1 kHz in artificial cerebrospinal fluid). Approximately 2 mm of the insulation was removed from the end of each electrode wire using a brief flame, and the de-insulated wires were soldered to separate sites on a 20-pin electrode connector. Two pairs of silver microwires (100 μm diameter, 99.95% pure) were

soldered onto the electrode connector as ground and reference electrodes. One end of the optical fiber was fixed onto a custom-made optical connector and stabilized on the electrode connector using a layer of epoxy.

In Vivo Electrophysiological Recording

Mice were anesthetized with urethane (10% *w/v*, 1.9 g/kg body weight) (Sigma) and secured in a stereotaxic apparatus. Scalp skin was removed and holes were drilled above the brain regions of interest. A multi-channel optrode array was inserted into the vlOFC (AP: 2.10 mm, ML: 1.50 mm, DV: 3.00–3.50 mm below dura) with the help of a stepping motor (IVM; Scientifica Ltd, Uckfield, UK) at 1 μm/s. The optic fiber was connected to the diode-pumped solid-state blue or yellow light laser. The power of the blue light was set at 10 mW–15 mW and the yellow light was set at 15 mW–20 mW at the tip of the fiber using a power meter (Thorlabs, Newton, MA) and the laser pulses were modified by an arbitrary/function generator (AFG3000B; Tektronix, Beaverton, OR). *In vivo* electrophysiological recording was performed using an OmniPlex® D Neural Data Acquisition System (Plexon, Dallas, TX). The continuous yellow laser to activate eNpHR3.0 and the 20-Hz 5 ms-pulsed blue laser to activate hChR2 was

Fig. 3 Fabrication of optogenetic probes and implant location. **A** Diagram of 16-channel optrode array. Each optrode contained an optical fiber for stimulation, and four tetrodes (16 channels) for electrical recording. **B, C** Location of optical stimulation and recording sites (arrowhead) in the vlOFC (scale bar, 750 μm).

452

Neurosci. Bull. June, 2019, 35(3):447–460
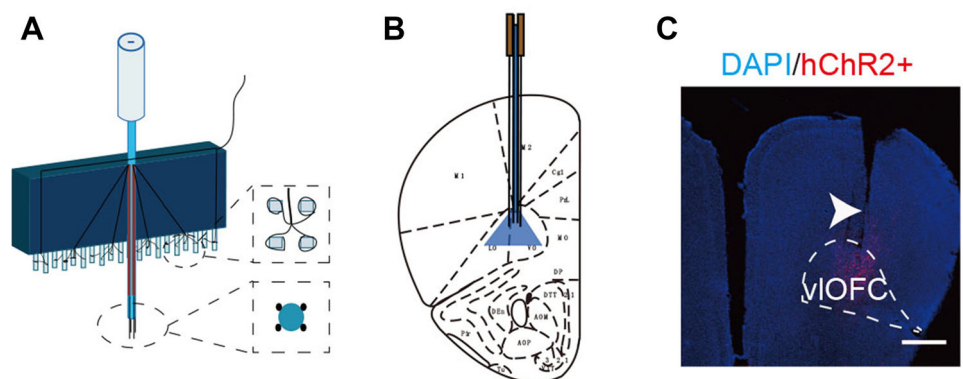
delivered when stable spontaneous spikes were recorded. At the end of experiments, the mice were sacrificed immediately and perfused transcardially.

In Vivo Neural Data Analysis

Neural data were analyzed with custom-written MATLAB scripts [31, 32]. The raw data were filtered through a second-order band-pass Butterworth filter of 300 Hz–3000 Hz to yield the spike train. Because the optical stimulation with blue or yellow light generated artifacts during recording, we used the Subtraction of Artifacts by Local Polynomial Approximation (SALPA) [33] algorithm to reduce their impact. The offline spike detection threshold was set at 3.5 standard deviations of the data stream [34]. Waveforms recorded from tetrodes and stereotrodes were analyzed according to the geometric configuration to yield reliable spike-sorting analysis. Next, probabilistic principal component analysis was used to decompose 12 principal components of the waveforms. Then a fuzzy c-means method was applied to pre-cluster the spike waveforms and the sorting was further aggregated based on a mixture of multivariate t-distributions algorithm [35]. For hChR2 activation of downstream neurons, peri-stimulus time histograms (PSTHs) were calculated with a bin size of 1 ms. The PSTHs of burst firing in response to blue light were calculated with a 50-ms bin size. For analysis of the inhibition of neural transmission by halorhodopsin, a bin size of 500 ms was used for the PSTHs.

Statistical Analyses

Data are expressed as mean $\pm$ SEM and were analyzed using SPSS 20.0 software (SPSS, Inc., Chicago, IL). Student's t-test or the paired t-test was used to determine the significance of differences between the means of two groups. Two-way analysis of variance (ANOVA) followed by post-hoc Bonferroni's multiple comparison test was performed to determine the significance of differences among groups. The level for significance was set at $P < 0.05$.

Results

The POR Consists of GABAergic and Glutamatergic Neurons

Previous studies have shown that the POR contains granule neurons and pyramidal neurons [21, 28]. However, the proportions of neurons in the mouse POR are unknown. Here, we confirmed the presence of GABAergic and glutamatergic neurons in the POR (Fig. 1E and F).

Furthermore, cell counts revealed that 48.4% $\pm$ 1.6% of POR neurons were GABAergic, while 51.4% $\pm$ 1.8% were glutamatergic (Fig. 1G).

### The POR–vlOFC Pathway is a Glutamatergic Structure

We verified that the POR contains almost equal proportions of inhibitory and excitatory neurons. We further mapped the connection between the POR and the vlOFC using engineered virus-delivered trackers. By injecting AAV5-CaMKIIα-mCherry into the POR of C57BL/6 mice [36], we observed the expression of mCherry in the vlOFC (Fig. 4A, B). But AAV5-DIO-mCherry in GAD2-cre mice did not show mCherry in the vlOFC (Fig. 4C, D). These results suggested that the POR–vlOFC pathway is a glutamatergic structure. However, the POR pathway terminates in multiple major areas including the visual area, LD, DHC, caudate-putamen, and vlOFC [22–24] (Fig. 4E). To determine if any other terminal structures of the POR pathway are glutamatergic, we visualized them using AAV5-CaMKIIα-mCherry as an anterograde tracer. We observed robust expression of mCherry in the vlOFC, LD, and DHC, but not in the caudate-putamen or visual area (Fig. 4F). These results verified that the vlOFC, LD, and DHC are major terminal areas of the glutamatergic pathway from the POR.

Glutamatergic POR Neurons Regulate Spatial Memory Retrieval

Previous studies have shown that the POR plays a role in spatial memory [37–39]. Here, we investigated the specific contribution of glutamatergic POR neurons to spatial memory by optogenetically stimulating these neurons in mice during novel object place recognition (Fig. 5A).

To determine whether inhibition of glutamatergic POR neurons hinders spatial memory, AAV5-CaMKIIα-eNpHR3.0-mCherry was injected into the bilateral POR (eNpHR3.0$^+$ group). Control animals were injected with AAV5-CaMKIIα-mCherry (mCherry$^+$ group). The mice were then exposed to two identical objects in the study phase to encourage spatial memory formation. After a delay, the position of one of the objects was changed. The mice were exposed to an original object and a "novel place" object with only location being changed to encourage the retrieval of spatial memory. The injected neurons were optically inhibited in either one or both phases (Fig. 5B, C). The mice showed no preference for either object in the study phase (paired t-test. Fig. 5D). A D2 score > 0 represents successful spatial memory performance and a higher D2 score means better performance. Two-way ANOVA for D2 using "group" (eNpHR3.0$^+$

Fig. 4 Anterograde tracing from the POR. **A–D** Anterograde tracing in C57BL/6 mice. AAV5–CaMKIIa–mCherry (red) was injected into the POR, and after 6 weeks the mCherry was predominant in the vlOFC, while using AAV5-DIO-mCherry in GAD2-Cre mice failed to show mCherry in the vlOFC (scale bars, 750 μm). **E** The major terminal areas of the pathway from the POR were the visual area (VIS), laterodorsal thalamic nucleus (LD), dorsal hippocampal commissure (DHC), caudate-putamen (CPu), and vlOFC. **F** Anterograde tracing in C57BL/6 mice. AAV5–CaMKIIa–mCherry (red) was injected into the POR, and after 6 weeks robust expression of mCherry was detected in the vlOFC, LD and DHC, but not in VIS and CPu (scale bar, 750 μm).
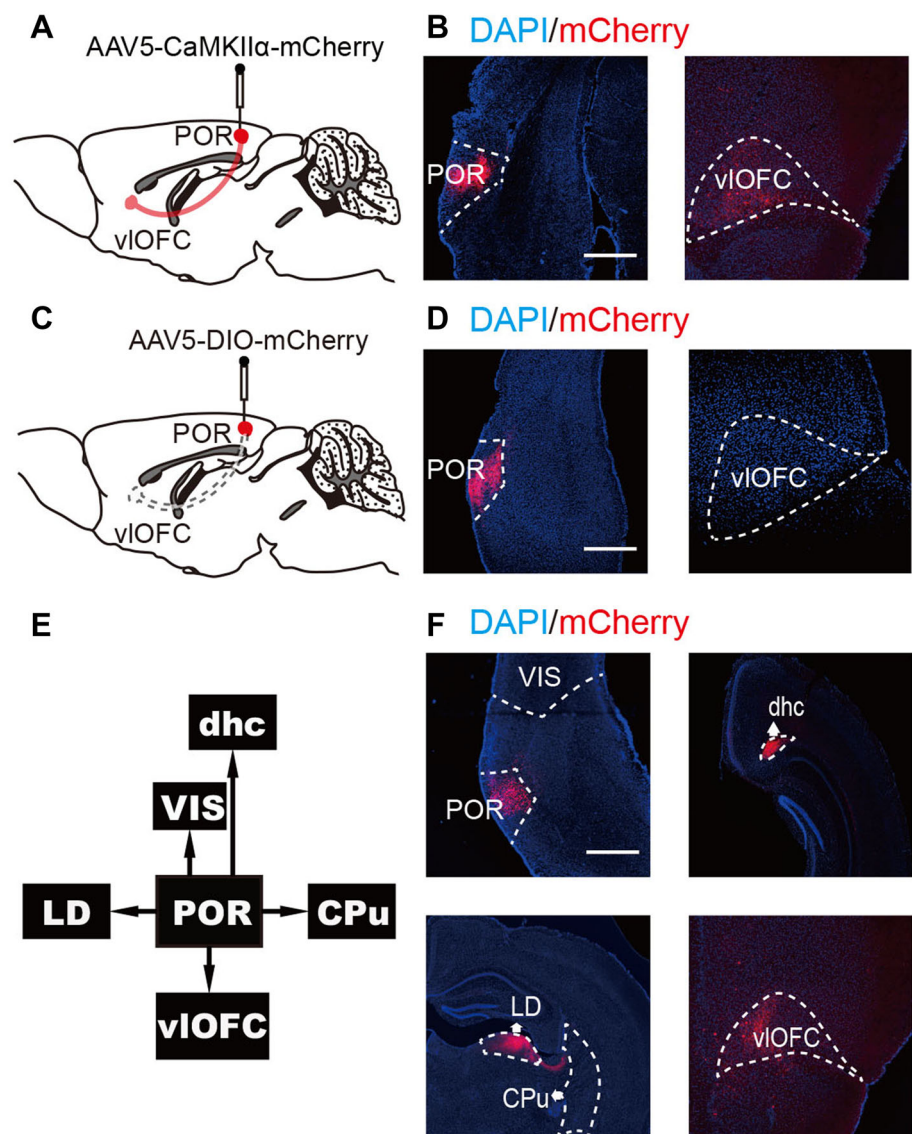
group or mCherry$^+$ group) and "optical stimulation" (stimulating in either one or both phases) revealed no significant interaction ($F(2, 37) = 1.617$, $P = 0.212$). Bonferroni *post-hoc* tests showed that the memory performance was significantly worse in the eNpHR3.0$^+$ group than in the control mCherry$^+$ group when optical stimulation was delivered only in the recognition phase (Fig. 5E, group 3: $P = 0.048$), suggesting that inhibiting glutamatergic neuronal activity in the POR impairs spatial memory retrieval. However, there was no significant difference in memory performance between the eNpHR3.0$^+$ and mCherry$^+$ groups when optical stimulation was delivered during both or the study phase (Fig. 5E, group 1: $P = 0.202$; group 2: $P = 0.638$), suggesting that the inhibition did not alter spatial memory retention.

To determine if activation of glutamatergic POR neurons improves spatial memory, AAV5-CaMKIIα-hChR2-mCherry was injected into the unilateral POR (hChR2$^+$ group). Control animals were injected with AAV5-CaMKIIα-mCherry (mCherry$^+$ group). The injected neurons were optically activated in either one or both phases (Fig. 5B and C). The mice showed no preference for either object in the study phase (paired *t*-test, Fig. 5F). A two-way ANOVA for D2 using group (hChR2$^+$ or mCherry$^+$ group) and optical stimulation (stimulating in either one or both phases) found no significant interaction (F (2, 33) = 1.147, $P = 0.330$). Bonferroni *post-hoc* tests showed no significant difference in memory performance between the hChR2$^+$ and mCherry$^+$ groups (Fig. 5G, group 4: $P = 0.127$; group 5: $P = 0.444$; group 6: $P = 0.600$), suggesting that spatial memory retention and retrieval were not affected.
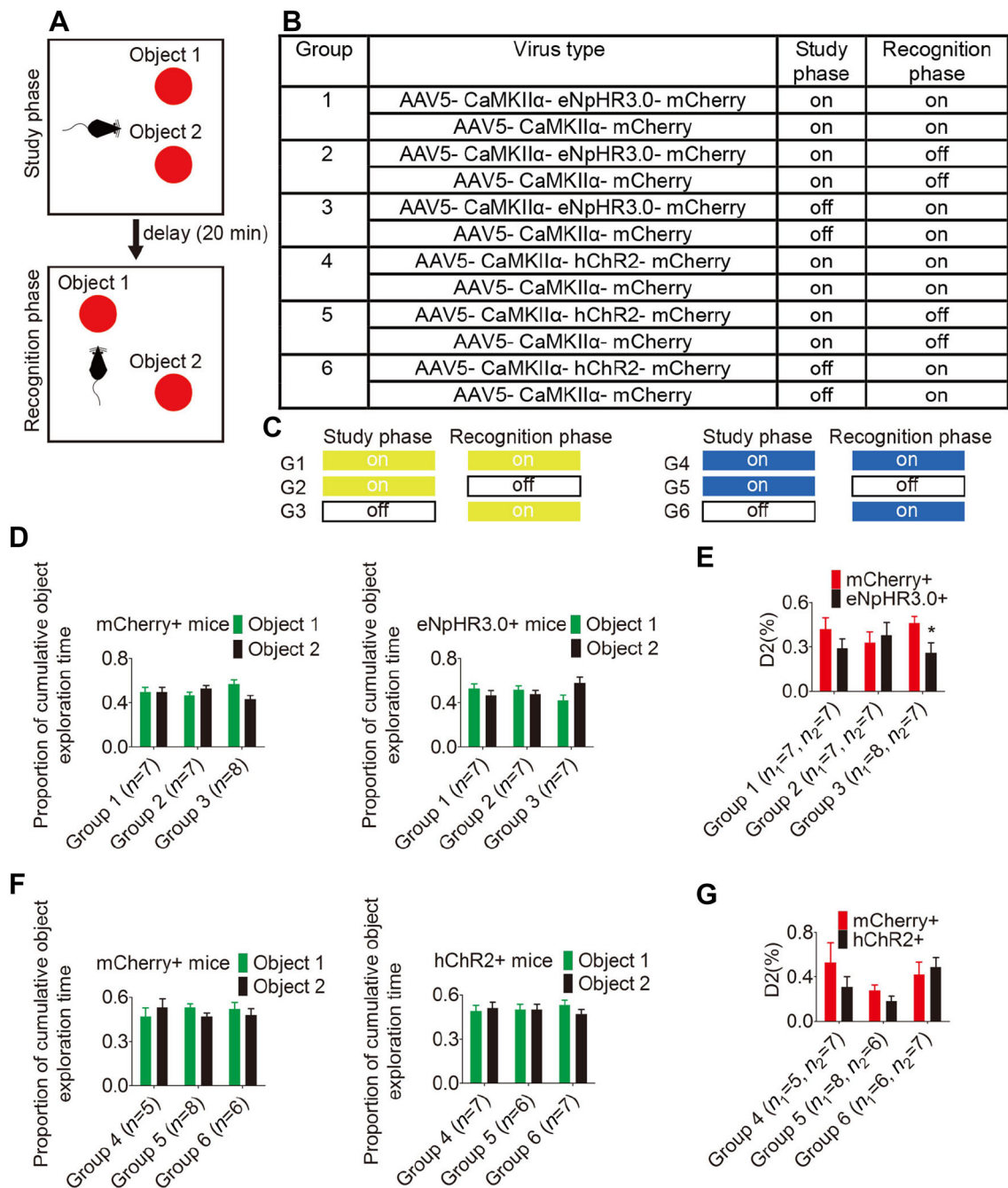
Fig. 5 Optogenetic inhibition of glutamatergic neurons in the POR impairs spatial memory. **A** Schematic of novel object place recognition test. **B**, **C** Animal groups and laser illumination protocol used during novel object place recognition. On: laser on, off: laser off, G1: Group 1. **D**, **F** Object exploration data in the study phase to objects 1 and 2 ($P < 0.05$ by paired t-test). **E**, **G** Comparison of D2 of mCherry$^+$ group and hChR2$^+$ group or eNpHR3.0$^+$ group (n_1: mCherry$^+$ group, n_2: hChR2$^+$ group or eNpHR3.0$^+$ group, *$P < 0.05$, Student's t-test). Data are presented as mean ± SEM.

Taken together, these data confirmed that glutamatergic neurons in the POR play an important role in spatial memory retrieval.

The POR–vlOFC Pathway Specifically Regulates Spatial Memory Retrieval

Based on the above findings, we further asked whether the POR regulates spatial memory retrieval through the vlOFC. To determine the role of the POR–vlOFC pathway in

Fig. 6 Implant locations of fibers and eNpHR3.0 expression in the terminal regions. **A–C** Locations of optical stimulation and eNpHR3.0 expression in the vlOFC, LD, and DHC (scale bars, 750 μm).
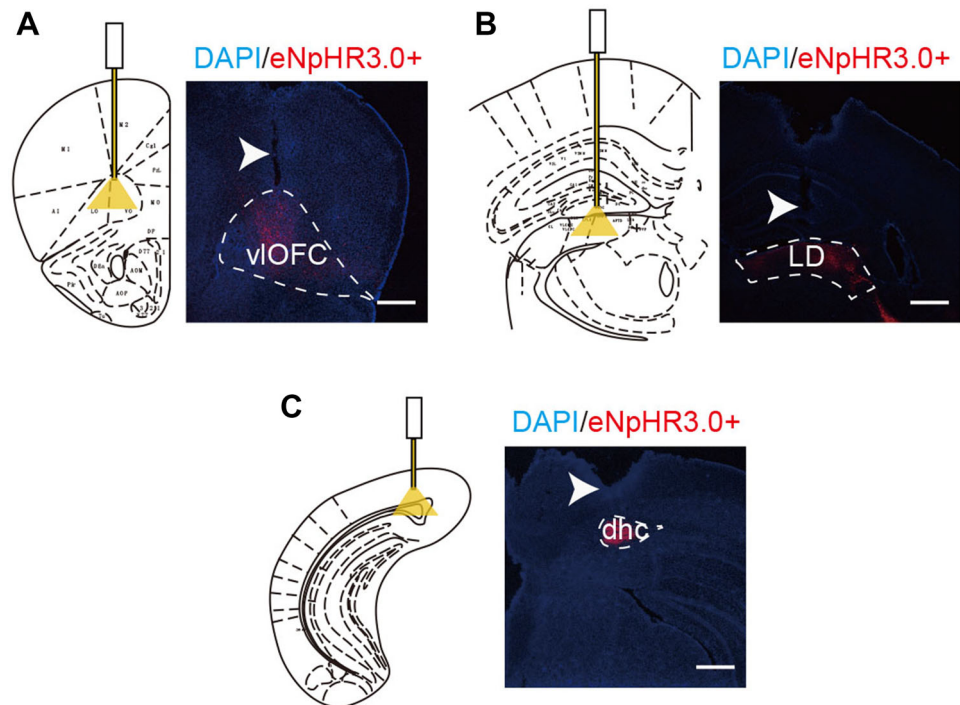
spatial memory, we optically inhibited the glutamatergic POR pathway terminals from each of the vlOFC, LD, and DHC during novel object place recognition in mice (Fig. 6A–C). AAV5-CaMKIIα-eNpHR3.0-mCherry was injected bilaterally into the POR (eNpHR3.0$^+$ group), and AAV5-CaMKIIα-mCherry was used as a control (mCherry$^+$ group). A yellow light stimulus was provided in these terminal areas in the recognition phase (Fig. 7A). Mice showed no preference for either object in the study phase (paired t-test; Fig. 7B). We found that the memory performance of the eNpHR3.0$^+$ group was worse than the control mCherry$^+$ group when optical stimulation was delivered to the vlOFC (Fig. 7C; $t = 2.283$, $P = 0.046$, Student's t-test), and there was no significant difference in memory performance between the eNpHR3.0$^+$ and mCherry$^+$ groups when the LD or DHC was optically stimulated (Fig. 7C; DHC: $t = 0.336$, $P = 0.744$; LD: $t = -0.212$, $P = 0.836$, Student's t-test). Subsequent to behavioral testing, the level of activity-dependent c-fos expression in the vlOFC was examined (Fig. 7D). The number of activated cells in response to the POR–vlOFC pathway was significantly lower in the eNpHR3.0$^+$ group than in the control mCherry$^+$ group (Fig. 7E; $t = 3.993$, $P = 0.016$, Student's t-test). Quantification of c-fos$^+$ neurons in the vlOFC revealed that $23.9\% \pm 1.5\%$ were GABAergic and $76.1\% \pm 1.5\%$ were glutamatergic (Fig. 7F–H). These findings suggest that inhibiting the POR–vlOFC pathway impairs spatial memory retrieval.

To measure the functional connection between the POR and the vlOFC, we used *in vivo* extracellular recordings in conjunction with optogenetic stimulation (Fig. 8A, D). After injecting the POR with AAV5-CaMKIIα-hChR2-mCherry, a 20-Hz blue light pulse with a 5-ms pulse width was used to stimulate the vlOFC. This terminal stimulation reliably elicited neuronal spiking, and 12/25 vlOFC cells responded to the stimulation at a latency of the peak response from 4 ms to 17 ms (average, 8.5 ± 1.12 ms) (Fig. 8B, C). To determine whether the pathway-specific glutamatergic input from the POR to the vlOFC contributes to the downstream firing of the vlOFC, AAV5-CaMKIIα-eNpHR3.0-mCherry was injected into the POR, and a continuous yellow light stimulus was delivered to vlOFC; this reduced the neuronal spiking (Fig. 8E, F). Taken together, the data suggested that the POR–vlOFC pathway specifically regulates spatial memory retrieval.

Discussion

In this study using AAV-delivered trackers, we found that the major terminal areas of the POR glutamatergic pathway are the vlOFC, LD, and DHC. Furthermore, we used *in vivo* optogenetic and electrophysiological methods, and c-fos staining to demonstrate that the POR–vlOFC pathway specifically transmits spatial information to participate in memory retrieval. Activation or inhibition of this pathway excited or inhibited the firing of postsynaptic neurons in the vlOFC. To the best of our knowledge, this is the first study to show that the POR–vlOFC pathway is a glutamatergic structure, and that it regulates spatial memory retrieval.
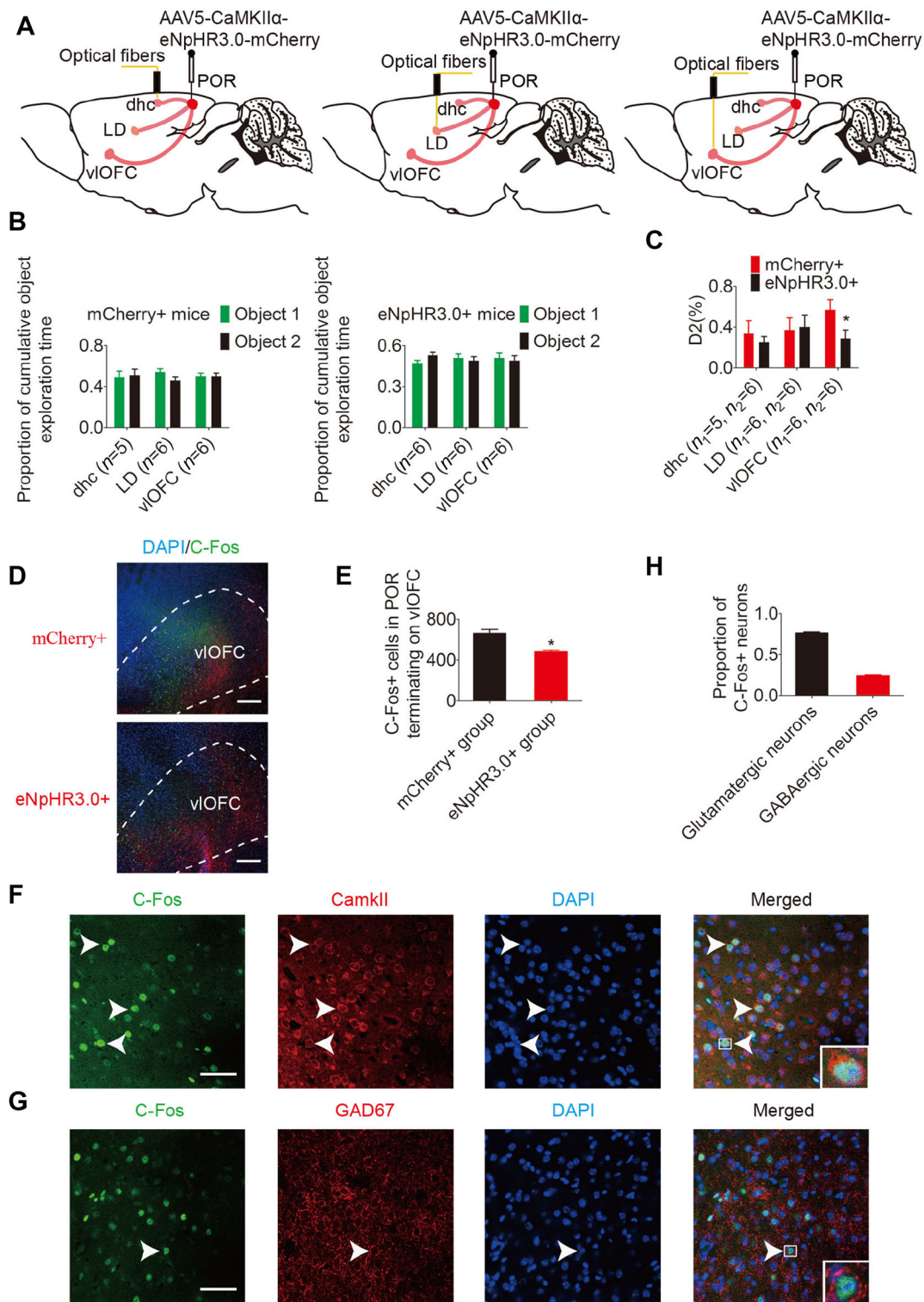
Fig. 7 The POR–vlOFC pathway specifically regulates spatial memory retrieval. **A** After POR injection of AAV5–CaMKIIa–mCherry (red), a yellow laser stimulus was delivered to each of the vlOFC, LD, and DHC. **B** Exploration of objects 1 and 2 in the study phase ($P < 0.05$, paired t-test). **C** Comparison of D2 in the mCherry[+] and eNpHR3.0[+] groups (n_1: mCherry[+] group, n_2: eNpHR3.0[+] group, *$P < 0.05$, Student's t-test). **D**, **E** C-fos + neurons (green) in the vlOFC after the yellow laser stimulus (scale bars, 250 μm; *$P < 0.05$, Student's t-test). **F**, **G** CamkII or GAD67 (red) stained with c-fos (green); arrowheads, co-labeled neurons (scale bars, 50 μm). **H** Proportions of GABAergic ($23.9\% \pm 1.5\%$) and glutamatergic ($76.1\% \pm 1.5\%$) c-fos^{+} neurons in the vlOFC. Data are presented as mean ± SEM.
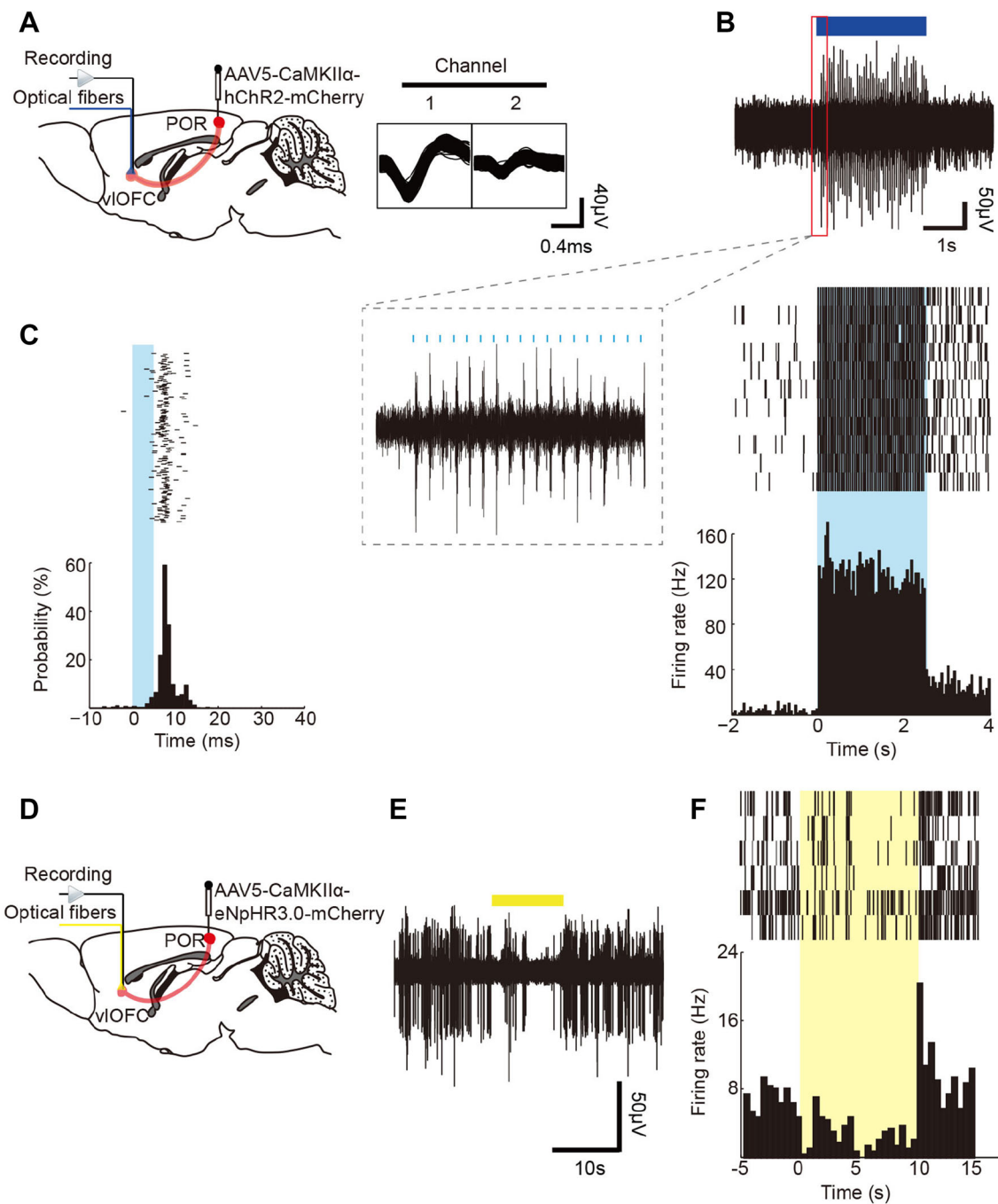
Fig. 8 Identification of functional connection from the POR to the vlOFC. **A** Schematic of POR injection of AAV5-CaMKIIα-hChR2-mCherry and vlOFC blue light stimulation, with representative traces for spikes (*n* = 12 cells). **B** Upper panel, example of vlOFC neurons responding to 20-Hz blue light stimulation of POR–vlOFC terminals; the insert (red) shows 18 light pulses (pulse width = 5 ms). Lower panels, representative raster plots and peri-stimulus time histogram (PSTH). **C** PSTH of a representative vlOFC neuron showing its response probability to a blue light stimulus. **D** Schematic of POR injection of AAV5-CaMKIIα-eNpHR3.0-mCherry and vlOFC yellow light stimulation. **E** Example of vlOFC neurons responding to continuous yellow light stimulation of POR–vlOFC terminals. **F** Representative raster plots and PSTH in response to yellow light stimulation. Data are presented as mean ± SEM.

Although the POR–vlOFC pathway has been investigated, its structure remained unclear. One of the major hindrances was the lack of high-precision techniques to dissect brain circuits. In recent years, neurotropic virus-

mediated tracing has become the most effective technology for circuit research. Compared with conventional tracers, the genetic recombinants of neurotropic viruses enable us to dissect the inputs and outputs of a specific brain region

458

Neurosci. Bull. June, 2019, 35(3):447–460

or cell type through multiple or single synaptic connections [40–42]. In previous studies [37, 43], the Morris water maze has been used as a classic behavioral test to study spatial memory. However, it can also be used to study episodic memory. Novel object place recognition is a memory test using the natural preference of rodents for new objects over familiar ones [29, 30, 44, 45]. Compared with the Morris water maze test, this behavioral test is considered a 'pure' spatial memory test because it is less likely to be disturbed by contextual information. Here, we used cell-type-specific tracing and *in vivo* optogenetic methods combined with novel object place recognition to determine that mice showed spatial memory impairment when the glutamatergic POR–vlOFC pathway was inhibited during the recognition phase of the behavioral test.

We found that the glutamatergic POR neurons regulate spatial memory retrieval. The POR is the rodent homolog of the primate parahippocampal cortex. Previous studies have hinted that the POR is involved in spatial memory [23, 37, 46], but its exact role is not well understood. Using single-unit recording, Furtak *et al.* found that the POR in rats encodes information related to the layout of objects in local contexts, regardless of their identity [47]. Furthermore, studies have suggested that the POR processes information about changes in the environment [48]. Bucci's team found that POR lesions in rodents alter performance in attentional orienting [49]. Another study showed that neuronal activity in the parahippocampal cortex of monkeys is altered by changes in the environment [50]. Furtak's group also found that location-selective cells in the POR are selective for location changes and postulated that the POR monitors the environmental context for changes and deploys attention to such changes [47]. That is, the POR participates in spatial memory retrieval and detects changes in the location of objects according to spatial feedback information. Our findings are the first to demonstrate that POR glutamatergic neurons play a role in spatial memory retrieval.

The UF is a long-range white-matter tract that originates in the temporal lobe, connecting the anterior temporal lobe with the OFC [8]. In rodents, the POR–vlOFC pathway may perform most UF functions [22]. Previous findings suggest that the UF is critically involved in some mnemonic functions [51–53]. In this study, we demonstrated that the POR–vlOFC pathway is glutamatergic. This pathway specifically transmits spatial information from the POR to the vlOFC to participate in memory retrieval. The OFC is located in the ventral surface of the prefrontal cortex. It receives inputs from visual, somatosensory, olfactory, auditory, and gustatory cortices [43]. There is evidence showing that it is a multimodal brain site for the convergence and integration of information [43, 54–56]. In spatial memory, some studies have shown that impairment

of the OFC in monkeys leads to failure in visual discrimination tasks [54]. In rats, previous research showed that OFC lesions impair the retention of spatial memory [43]. The OFC may be a 'relay station' for receiving and reprocessing spatial information. As a white matter tract connecting the POR with the vlOFC, the POR–vlOFC pathway was found to transmit spatial information encoded in the POR to the vlOFC for further reprocessing in spatial memory retrieval.

The present study has some limitations. First, although the function of the POR–vlOFC pathway in spatial memory retrieval was clarified, the neural circuits for encoding and storing spatial memory remain to be analyzed in detail. Second, we investigated the POR–vlOFC pathway only in mice; studies in primates are needed to confirm these initial findings, and studies of animal models of AD are needed to determine whether the POR–vlOFC pathway is impaired in MCI and AD, particularly, animal models with spatial memory retrieval damage.

In summary, our findings have identified a prominent excitatory pathway from the POR to the vlOFC that specifically transmits spatial information to regulate spatial memory retrieval. These findings may provide a better understanding of the function and dysfunction of the uncinate fasciculus in neurological disorders, such as MCI and AD.

Conflict of interest All authors declare that no competing interests exist.

References

1. Madl T, Chen K, Montaldi D, Trappl R. Computational cognitive models of spatial memory in navigation space: A review. Neural Netw 2015, 65: 18–43.
2. Siedlecki KL, Salthouse TA. Using contextual analysis to investigate the nature of spatial memory. Psychon Bull Rev 2014, 21: 721–727.
3. Iachini I, Iavarone A, Senese VP, Ruotolo F, Ruggiero G. Visuospatial memory in healthy elderly, AD and MCI: a review. Curr Aging Sci 2009, 2: 43–59.
4. Kunz L, Schröder TN, Lee H, Montag C, Lachmann B, Sariyska R, *et al.* Reduced grid-cell-like representations in adults at genetic risk for Alzheimer's disease. Science 2015, 350: 430–433.
5. Wei EX, Oh ES, Harun A, Ehrenburg M, Agrawal Y. Vestibular loss predicts poorer spatial cognition in patients with Alzheimer's disease. J Alzheimers Dis 2018, 61: 995–1003.

6. Ranganath C. Working memory for visual objects: complementary roles of inferior temporal, medial temporal, and prefrontal cortex. Neuroscience 2006, 139: 277–289.

7. Mohr HM, Goebel R, Linden DE. Content- and task-specific dissociations of frontal activity during maintenance and manipulation in visual working memory. J Neurosci 2006, 26: 4465–4471.

8. Von Der Heide RJ, Skipper LM, Klobusicky E, Olson IR. Dissecting the uncinate fasciculus: disorders, controversies and a hypothesis. Brain 2013, 136: 1692–1707.

9. Thiebaut de Schotten M, Dell'Acqua F, Valabregue R, Catani M. Monkey to human comparative anatomy of the frontal lobe association tracts. Cortex 2012, 48: 82–96.

10. Lebel C, Beaulieu C. Longitudinal development of human brain wiring continues from childhood into adulthood. J Neurosci 2011, 31: 10937–10947.

11. Phan KL, Orlichenko A, Boyd E, Angstadt M, Coccaro EF, Liberzon I, et al. Preliminary evidence of white matter abnormality in the uncinate fasciculus in generalized social anxiety disorder. Biol Psychiatry 2009, 66: 691–694.

12. Riva-Posse P, Choi KS, Holtzheimer PE, McIntyre CC, Gross RE, Chaturvedi A, et al. Defining critical white matter pathways mediating successful subcallosal cingulate deep brain stimulation for treatment-resistant depression. Biol Psychiatry 2014, 76: 963–969.

13. Ćurčić-Blake B, Nanetti L, van der Meer L, Cerliani L, Renken R, Pijnenborg GH, et al. Not on speaking terms: hallucinations and structural network disconnectivity in schizophrenia. Brain Struct Funct 2015, 220: 407–418.

14. Craig MC, Catani M, Deeley Q, Latham R, Daly E, Kanaan R, et al. Altered connections on the road to psychopathy. Mol Psychiatry 2009, 14: 946–953, 907.

15. Mahoney CJ, Simpson IJ, Nicholas JM, Fletcher PD, Downey LE, Golden HL, et al. Longitudinal diffusion tensor imaging in frontotemporal dementia. Ann Neurol 2015, 77: 33–46.

16. Douaud G, Jbabdi S, Behrens TE, Menke RA, Gass A, Monsch AU, et al. DTI measures in crossing-fibre areas: increased diffusion anisotropy reveals early white matter alteration in MCI and mild Alzheimer's disease. Neuroimage 2011, 55: 880–890.

17. Villain N, Fouquet M, Baron JC, Mézenge F, Landeau B, de La Sayette V, et al. Sequential relationships between grey matter and white matter atrophy and brain metabolic abnormalities in early Alzheimer's disease. Brain 2010, 133: 3301–3314.

18. Korthauer LE, Nowak NT, Moffat SD, An Y, Rowland LM, Barker PB, et al. Correlates of virtual navigation performance in older adults. Neurobiol Aging 2016, 39: 118–127.

19. Wu YF, Wu WB, Liu QP, He WW, Ding H, Nedelska Z, et al. Presence of lacunar infarctions is associated with the spatial navigation impairment in patients with mild cognitive impairment: a DTI study. Oncotarget 2016, 7: 78310–78319.

20. Delatour B, Witter MP. Projections from the parahippocampal region to the prefrontal cortex in the rat: evidence of multiple pathways. Eur J Neurosci 2002, 15: 1400–1407.

21. Beaudin SA, Singh T, Agster KL, Burwell RD. Borders and comparative cytoarchitecture of the perirhinal and postrhinal cortices in an F1 hybrid mouse. Cereb Cortex 2013, 23: 460–476.

22. Delatour B, Witter MP. Projections from the parahippocampal region to the prefrontal cortex in the rat: evidence of multiple pathways. Eur J Neurosci 2002, 15: 1400–1407.

23. Agster KL, Burwell RD. Cortical efferents of the perirhinal, postrhinal, and entorhinal cortices of the rat. Hippocampus 2009, 19: 1159–1186.

24. Allen-Brain-Atlas. Mouse Connectivity. Available from http://connectivity.brain-map.org/.

25. Liu P, Bilkey DK. The effects of NMDA lesions centered on the postrhinal cortex on spatial memory tasks in the rat. Behav Neurosci 2002, 116: 860–873.

26. Vafaei AA, Rashidy-Pour A. Reversible lesion of the rat's orbitofrontal cortex interferes with hippocampus-dependent spatial memory. Behav Brain Res 2004, 149: 61-68.

27. Abdel-Aal RA, Assi AA, Kostandy BB. Memantine prevents aluminum-induced cognitive deficit in rats. Behav Brain Res 2011, 225: 31–38.

28. Sills JB, Connors BW, Burwell RD. Electrophysiological and morphological properties of neurons in layer 5 of the rat postrhinal cortex. Hippocampus 2012, 22: 1912–1922.

29. Beer Z, Chwiesko C, Kitsukawa T, Sauvage MM. Spatial and stimulus-type tuning in the LEC, MEC, POR, PrC, CA1, and CA3 during spontaneous item recognition memory. Hippocampus 2013, 23: 1425–1438.

30. Boyce R, Glasgow SD, Williams S, Adamantidis A. Causal evidence for the role of REM sleep theta rhythm in contextual memory consolidation. Science 2016, 352: 812–816.

31. Taylor IM, Du Z, Bigelow ET, Eles JR, Horner AR, Catt KA, et al. Aptamer-functionalized neural recording electrodes for the direct measurement of cocaine in vivo. J Mater Chem B Mater Biol Med 2017, 5: 2445–2458.

32. Du ZJ, Luo X, Weaver C, Cui XT. Poly (3, 4-ethylenedioxythiophene)-ionic liquid coating improves neural recording and stimulation functionality of MEAs. J Mater Chem C Mater Opt Electron Devices 2015, 3: 6515–6524.

33. Wagenaar DA, Potter SM. Real-time multi-channel stimulus artifact suppression by local curve fitting. J Neurosci Methods 2002, 120: 113–120.

34. Ludwig KA, Uram JD, Yang J, Martin DC, Kipke DR. Chronic neural recordings using silicon microelectrode arrays electrochemically deposited with a poly(3,4-ethylenedioxythiophene) (PEDOT) film. J Neural Eng 2006, 3: 59–70.

35. Shoham S, Fellows MR, Normann RA. Robust, automatic spike sorting using mixtures of multivariate t-distributions. J Neurosci Methods 2003, 127: 111–122.

36. Yang Y, Wang Z, Jin S, Gao D, Liu N, Chen S, et al. Opposite monosynaptic scaling of BLP-vCA1 inputs governs hopefulness- and helplessness-modulated spatial learning and memory. Nat Commun 2016, 7: 11935.

37. Liu P, Bilkey DK. The effects of NMDA lesions centered on the postrhinal cortex on spatial memory tasks in the rat. Behav Neurosci 2002, 116: 860–873.

38. Ramos JM. Differential contribution of hippocampus, perirhinal cortex and postrhinal cortex to allocentric spatial memory in the radial maze. Behav Brain Res 2013, 247: 59–64.

39. Zhang GR, Cao H, Kong L, O'Brien J, Baughns A, Jan M, et al. Identified circuit in rat postrhinal cortex encodes essential information for performing specific visual shape discriminations. Proc Natl Acad Sci U S A 2010, 107: 14478–14483.

40. Boldogkoi Z, Balint K, Awatramani GB, Balya D, Busskamp V, Viney TJ, et al. Genetically timed, activity-sensor and rainbow transsynaptic viral tools. Nat Methods 2009, 6: 127–130.

41. McCarty DM. Self-complementary AAV vectors; advances and applications. Mol Ther 2008, 16: 1648–1656.

42. Betley JN, Sternson SM. Adeno-associated viral vectors for mapping, monitoring, and manipulating neural circuits. Hum Gene Ther 2011, 22: 669–677.

43. Vafaei AA, Rashidy-Pour A. Reversible lesion of the rat's orbitofrontal cortex interferes with hippocampus-dependent spatial memory. Behav Brain Res 2004, 149: 61–68.

44. Ennaceur A, Delacour J. A new one-trial test for neurobiological studies of memory in rats. 1: Behavioral data. Behav Brain Res 1988, 31: 47–59.

45. Clarke JR, Cammarota M, Gruart A, Izquierdo I, Delgado-Garcia JM. Plastic modifications induced by object recognition memory processing. Proc Natl Acad Sci U S A 2010, 107: 2652–2657.

46. Burgess N, Maguire EA, Spiers HJ, O'Keefe J. A temporoparietal and prefrontal network for retrieving the spatial context of lifelike events. Neuroimage 2001, 14: 439–453.

47. Furtak SC, Ahmed OJ, Burwell RD. Single neuron activity and theta modulation in postrhinal cortex during visual object discrimination. Neuron 2012, 76: 976–988.

48. Suter EE, Weiss C, Disterhoft JF. Perirhinal and postrhinal, but not lateral entorhinal, cortices are essential for acquisition of trace eyeblink conditioning. Learn Mem 2013, 20: 80–84.

49. Bucci DJ, Burwell RD. Deficits in attentional orienting following damage to the perirhinal or postrhinal cortices. Behav Neurosci 2004, 118: 1117–1122.

50. Vidyasagar TR, Salzmann E, Creutzfeldt OD. Unit activity in the hippocampus and the parahippocampal temporobasal association cortex related to memory and complex behaviour in the awake monkey. Brain Res 1991, 544: 269–278.

51. Mayo CD, Mazerolle EL, Ritchie L, Fisk JD, Gawryluk JR. Longitudinal changes in microstructural white matter metrics in Alzheimer's disease. Neuroimage Clin 2017, 13: 330–338.

52. O'Dwyer L, Lamberton F, Bokde AL, Ewers M, Faluyi YO, Tanner C, *et al.* Multiple indices of diffusion identifies white matter damage in mild cognitive impairment and Alzheimer's disease. PLoS One 2011, 6: e21745.

53. Li W, Muftuler LT, Chen G, Ward BD, Budde MD, Jones JL, *et al.* Effects of the coexistence of late-life depression and mild cognitive impairment on white matter microstructure. J Neurol Sci 2014, 338: 46–56.

54. Zald DH, Kim SW. Anatomy and function of the orbital frontal cortex, I: anatomy, neurocircuitry; and obsessive-compulsive disorder. J Neuropsychiatry Clin Neurosci 1996, 8: 125–138.

55. Petrides M. The orbitofrontal cortex: novelty, deviation from expectation, and memory. Ann N Y Acad Sci 2007, 1121: 33–53.

56. Swanson A, Allen A, Shapiro L, Gourley S. GABAAα1-mediated plasticity in the orbitofrontal cortex regulates context-dependent action selection. Neuropsychopharmacology 2015, 40: 1027–1036.